



# Improving intrinsic oxygen reduction activity and stability: Atomic layer deposition preparation of platinum-titanium alloy catalysts

Yongmin Kim<sup>a,b</sup>, Shicheng Xu<sup>a</sup>, Joonsuk Park<sup>c</sup>, Anup Lal Dadlani<sup>a</sup>, Olga Vinogradova<sup>d</sup>, Dilip Krishnamurthy<sup>e</sup>, Marat Orazov<sup>f</sup>, Dong Un Lee<sup>f</sup>, Sam Dull<sup>f</sup>, Peter Schindler<sup>c</sup>, Hyun Soo Han<sup>a</sup>, Zhaoxuan Wang<sup>c</sup>, Tanja Graf<sup>g</sup>, Thomas D. Schladt<sup>g</sup>, Jonathan E. Mueller<sup>g</sup>, Ritimukta Sarangi<sup>h</sup>, Ryan Davis<sup>h</sup>, Venkatasubramanian Viswanathan<sup>d,\*</sup>, Thomas Francisco Jaramillo<sup>f,\*</sup>, Drew C. Higgins<sup>f,i,\*\*</sup>, Fritz B. Prinz<sup>a,c,j,\*\*\*</sup>

<sup>a</sup> Department of Mechanical Engineering, Stanford University, Stanford, CA 94305, USA

<sup>b</sup> Center for Hydrogen-Fuel Cell Research, Korea Institute of Science and Technology, Seoul 02792, Republic of Korea

<sup>c</sup> Department of Material Science and Engineering, Stanford University, Stanford, CA 94305, USA

<sup>d</sup> Department of Chemical Engineering, Carnegie Mellon University, Pittsburgh, PA 15213, USA

<sup>e</sup> Department of Mechanical Engineering, Carnegie Mellon University, Pittsburgh, PA 15213, USA

<sup>f</sup> Department of Chemical Engineering, Stanford University, Stanford, CA 94305, USA

<sup>g</sup> Volkswagen Group Research, Wolfsburg, Germany

<sup>h</sup> Stanford Synchrotron Radiation Lightsource, SLAC National Accelerator Laboratory, 2575 Sand Hill Road, Menlo Park, CA 94025, USA

<sup>i</sup> Department of Chemical Engineering, McMaster University, Hamilton, ON, Canada

<sup>j</sup> Department of Mechanical and Industrial Engineering, Norwegian University of Science and Technology, Trondheim, Norway

## ARTICLE INFO

### Keywords:

Atomic layer deposition  
Polymer electrolyte fuel cells  
Oxygen reduction reaction  
Platinum–titanium alloys

## ABSTRACT

Improved activity and stability Pt-based catalysts for the oxygen reduction reaction (ORR) are needed to perpetuate the deployment of polymer electrolyte fuel cells (PEFCs) in the transportation sector. Here, we use atomic layer deposition of TiO<sub>2</sub> and Pt coupled with thermal reductive annealing to prepare Pt<sub>3</sub>Ti electrocatalysts. The atomic level synthetic control resulted in Pt<sub>3</sub>Ti nanoparticles with high ORR performance, including a mass activity of 1.84 A/mg<sub>Pt</sub> and excellent electrochemical stability. The Pt<sub>3</sub>Ti nanoparticles show excellent specific activity — 5.3-fold higher than commercial Pt/C and 3-fold higher than polycrystalline Pt, exceeding the performance of any PtTi catalysts reported to date. Combined experimental and computational efforts indicate that Pt enrichment on the Pt<sub>3</sub>Ti enhances the activity, and the intrinsic stability of the Pt<sub>3</sub>Ti phase provides durability. This knowledge, along with the facile fabrication of alloys by atomic layer deposition, can be leveraged to designed improved performance catalysts.

## 1. Introduction

Polymer electrolyte fuel cell (PEFC) technologies are complementary to battery technologies as they are capable of providing sustainable electrification of the transport sector, while allowing for extended driving range and fast refueling times. However, the use of expensive Pt group metals as electrocatalysts in PEFCs currently creates a cost barrier towards the widespread commercialization of this technology, and

electrocatalyst stability is still insufficient for desired long-term operation. Therefore, considerable efforts in electrocatalyst and electrode R&D has focused on reducing Pt contents and improving catalyst stability, bolstered by supports from the Fuel Cell Technologies Office within the U.S. Department of Energy (DOE) [1]. Specifically, significant emphases have been placed on developing cathode catalysts for the oxygen reduction reaction (ORR), which is intrinsically kinetically sluggish and accounts for the greatest potential losses. A significant

\* Corresponding authors.

\*\* Correspondence to: Department of Chemical Engineering, McMaster University, Hamilton, ON L8S 4L8, Canada.

\*\*\* Corresponding author at: Department of Mechanical Engineering, Stanford University, Stanford, CA 94305, USA.

E-mail addresses: [venkvis@cmu.edu](mailto:venkvis@cmu.edu) (V. Viswanathan), [jaramillo@stanford.edu](mailto:jaramillo@stanford.edu) (T.F. Jaramillo), [higgid2@mcmaster.ca](mailto:higgid2@mcmaster.ca) (D.C. Higgins), [fprinz@stanford.edu](mailto:fprinz@stanford.edu) (F.B. Prinz).

<https://doi.org/10.1016/j.apcatb.2021.120741>

Received 1 July 2021; Received in revised form 27 August 2021; Accepted 17 September 2021

Available online 22 September 2021

0926-3373/© 2021 Elsevier B.V. All rights reserved.

portion of Pt-based ORR catalyst development efforts involve either the development of Pt catalysts with ultrahigh dispersion [2] or Pt-based catalysts (Pt alloy or core-shell (Pt) structured catalysts) to improve the ORR activity through electronic perturbations [3–8], or the development of corrosion-resistant (i.e.,  $\text{TiO}_2$ ,  $\text{Nb}_2\text{O}_5$ ,  $\text{SnO}_2$ ,  $\text{TiN}$ ) Pt nanoparticle supports to improve both activity and stability [9–13]. A key challenge facing the development of Pt-alloy catalysts is the intrinsic instability of the most commonly used base metals (i.e., Co, Ni, Fe) that will undergo dissolution under PEFC operating conditions, resulting in a loss of the activity enhancements gained through alloying and reducing the proton conductivity of the ionomer and electrolyte [14].

In an attempt to identify improved activity of ORR electrocatalysts without compromised stability, studies involving computational screening of various Pt- and Pd-alloys have taken into account alloy formation energies as a descriptor for stability and oxygen adsorption energies as a descriptor for activity [4]. Supplemented by experimental investigations, this study successfully led to the discovery of  $\text{Pt}_3\text{Y}$  and  $\text{Pt}_3\text{Sc}$  as highly active and stable catalysts for the ORR. Subsequent efforts have extended to include other Pt-lanthanide alloys [5], however, translating these concepts towards the development of practical nanoparticle catalysts has been challenging owing to the high oxo-philicity of the lanthanide series metals [15].  $\text{Pt}_3\text{Ti}$  was also identified computationally as a potentially active and intrinsically stable alloy composition, with an alloy formation energy of ca.  $-0.80$  eV — significantly more negative than the most commonly used Pt-Co and Pt-Ni alloys (ca.  $-0.01$  eV and  $-0.10$  eV) [4]. Accordingly, minimal dissolution of the Ti component of these alloys and the thermodynamic stability of the  $\text{Pt}_3\text{Ti}$  phase presents an advantage over conventionally used PtNi or PtCo alloys, where the base metal (i.e., Ni or Co) dissolution presents a thermodynamic limitation on stability that has been very challenging to overcome [16,17]. Furthermore, Ti is generally less oxo-philic than lanthanide metals and therefore more amenable to straightforward synthetic approaches (bond dissociation energies of Ti-O, Gd-O, and Y-O are 662, 716, and 715.1 kJ/mol, respectively [18]). Researchers have experimentally evaluated the ORR activity of a series of polycrystalline  $\text{Pt}_3\text{M}$  electrodes ( $\text{M} = \text{Ti}, \text{V}, \text{Fe}, \text{Co}, \text{Ni}$ ), whereby a negligible improvement was demonstrated for  $\text{Pt}_3\text{Ti}$  in comparison to polycrystalline Pt [3]. This was explained computationally by the  $\text{Pt}_3\text{Ti}$  surface having binding energies with adsorbed reaction intermediates (i.e.,  $\text{OOH}^*$ ,  $\text{O}^*$ ,  $\text{OH}^*$ ), weaker than optimal for ORR. This limitation can be addressed by tuning the alloy configuration in the near-surface region [4] or through nano-structuring effects inducing stronger oxygen adsorption energies by under-coordinated surface sites in nanoparticulates [19–22]. However, the preparation of  $\text{Pt}_3\text{Ti}$  nanoparticles has still been challenging using traditional synthetic approaches, largely due to the significantly different reversible potentials for the reduction of Pt vs. Ti ions ( $\text{Pt}^{2+} + 2\text{e}^- \rightarrow \text{Pt}(\text{s})$  at  $+1.18$  eV vs. RHE,  $\text{Ti}^{2+} + 2\text{e}^- \rightarrow \text{Ti}(\text{s})$  at  $-1.6$  eV vs. RHE, Ref. [23]) that lead to difficulties achieving alloying between these two metals [24].

To address this challenge, we report the use of atomic layer deposition (ALD) of Pt and  $\text{TiO}_2$  in combination with a subsequent reduction step to prepare Pt-Ti alloys. Particularly, ALD is a well-established process for deposition of Pt [11,25–27] and  $\text{TiO}_2$  [11,28,29], and is an attractive approach as it provides atomic level control over the deposition of each individual component [30,31]. Furthermore, our group [25] and others [32] have demonstrated ALD is capable of preparing Pt nanoparticles on high surface area support materials. In this work, we use ALD to deposit  $\text{TiO}_2$  onto carbon-based substrates followed by ALD of Pt to exploit the affinity of Pt ALD precursors towards  $\text{TiO}_2$  surfaces [33]. This affinity ensures that Pt and  $\text{TiO}_2$  are in close contact, and due to the strong metal support interactions between Pt and  $\text{TiO}_2$  [34], enables facile Pt-Ti alloy formation through a subsequent thermal treatment in  $\text{H}_2$ . Through this approach, we successfully synthesize highly active  $\text{Pt}_3\text{Ti}$  nanoparticle catalysts with a specific activity  $\sim 3\times$  higher than that of polycrystalline Pt, and a mass activity more than two-fold higher than pure Pt nanoparticles prepared by ALD or commercial Pt

nanoparticle catalysts supported on Vulcan carbon black (Pt/Vulcan) — activity enhancement factors that exceed those reported previously for Pt-Ti catalysts. The process of  $\text{Pt}_3\text{Ti}$  alloy formation through ALD and thermal annealing to gain insight into the structural evolution of the catalysts during synthesis was tracked using high resolution transmission electron microscopy (HRTEM), X-ray photoelectron spectroscopy (XPS), and X-ray absorption spectroscopy (XAS). The resulting catalyst properties were also extensively characterized using HRTEM, XAS and secondary ion mass spectroscopy (SIMS) to probe the electronic structure and atomic configuration of Pt and Ti atoms within the catalyst. We employ density functional theory (DFT) correlated with results from this rigorous structural characterization to develop a mechanistic understanding of the activity and stability enhancements observed for  $\text{Pt}_3\text{Ti}$  that is currently missing in the scientific literature. The excellent performance of ALD-prepared  $\text{Pt}_3\text{Ti}$  combined with the newly developed scientific understanding of the performance-structure-property relationship of this alloy system can guide the further development of bimetallic electrocatalysts for ORR with improved activity and stability.

## 2. Experimental

### 2.1. Preparation of samples (Pt/GC and Pt/ $\text{TiO}_2$ /GC catalysts)

Glassy carbon (GC) disks with one side polished (diameter, 5 mm; thickness, 4 mm; SIGRADUR®; HTW chemicals; root-mean-squared (RMS) roughness =  $\sim 1.9$  nm) were chosen to be substrates for catalysts. GC disks with the excellent thermal resistance are appropriate as model substrates since they exhibit very low oxygen reduction reaction (ORR) activities due to lack of defects and chemical functionalities, and thus provide a suitable means for evaluating catalytic activity [25]. Plasma enhanced atomic layer deposition (PEALD) was used to fabricate Pt/GC and Pt/ $\text{TiO}_2$ /GC catalysts as well as all other samples used for materials characterization. PEALD was performed in the FlexAL system (Oxford instruments) equipped with a remote inductively coupled plasma (ICP) operating at 13.56 MHz and a turbo pump leading to the base pressure of the reactor to be  $10^{-7}$ – $10^{-5}$  Torr. All depositions were conducted at a substrate temperature of  $250^\circ\text{C}$ . Prior to the ALD deposition, the GC substrates was pre-treated with oxygen plasma to remove organic contaminants as well as increasing oxygen-containing functional groups essential for ALD growth. Trimethyl(methylcyclopentadienyl) platinum (IV) ( $\text{MeCpPtMe}_3$ , 99%, Strem Chemicals) and tetrakis(dimethylamido) titanium ( $[(\text{CH}_3)_2\text{N}]_4\text{Ti}$ , Sigma Aldrich) were utilized as the Pt and Ti precursors. Temperature and dosing time are two crucial parameters for ALD precursors to maintain the chemical stability of precursors while ensuring optimal delivery of precursor needed for the ALD growth. The precursor cylinders of both Pt and Ti precursors were heated to  $65^\circ\text{C}$  and the dosing times for precursors were controlled to maintain precursor pressures above 25 mTorr during the precursor saturation step after the precursor dosing step. Oxygen plasma was generated from the ICP generator (plasma power, 300 W; operating pressure, 40 mTorr). Table S2 shows the detailed processing times for each step for Pt and  $\text{TiO}_2$  PEALDs. Hydrogen post-thermal annealing was conducted at a tube furnace and the inner tube pressure was maintained at a pressure of  $\sim 40$  mTorr while continually flowing hydrogen (99.999%, Praxair) into the reactor. The ramping rate and the dwelling time at a particular temperature were set to be  $10^\circ\text{C}/\text{min}$  and 5 min, respectively. The thermal stability of the GC support at the elevated temperatures was confirmed and there was no significant loss of ALD Pt induced by possible reaction between  $\text{H}_2$  and the GC.

### 2.2. Electrochemical testing

#### 2.2.1. ORR testing setup

A three-electrode electrochemical cell equipped with rotation electrode disk (RDE) as a working electrode, platinum wire as a counter

electrode, reversible-hydrogen electrode (RHE) as a reference electrode was used. All catalyst samples were assembled in the “ChangeDisk RDE tips” (model number, AFE4TQ050; manufacturer, Pine Research Instrumentation(PRI)): ALD-catalyst-coated GC disks (outer diameter, 5 mm) were pushed into the annular disk holder (model number, ACE4THQ050; materials, PTFE; inner diameter, 5 mm; manufacturer, PRI) until the bottom of the GC disks reached an electrical contact (model number, ACE4TVP; manufacturer, PRI). During the insertion, the catalyst-coated surfaces were protected by polypropylene films (model number, 102680P1A; manufacturer, CHEMPLEX). The cylindrical PTFE body holding the catalyst-coated-GC disks were then assembled with the RDE shaft (model number, AFE3M; manufacturer, PRI) of the MSR electrode rotator (manufacturer, PRI) for the RDE testing. The RDE testing protocol is in accordance with the previously published method [35]. Before electrochemical testing, all glassware and Teflon parts were cleaned by piranha solution overnight. 0.1 M HClO<sub>4</sub> solution was used as an electrolyte, which was prepared by diluting 70% HClO<sub>4</sub> aqueous solution (Merck, Suprapur) with ultrapure deionized water (18.2 MΩ cm, TOC < 5 ppb). All the gases used in this study were ultrapure grade (supplier, Praxair; purity, 99.9999% (Ar), 99.999% (O<sub>2</sub>), 99.999% (H<sub>2</sub>)).

### 2.2.2. ORR testing protocols

The measurement temperature was kept at  $23 \pm 2$  °C. Electrochemical testing was conducted using a Solartron Voltameter-Impedance analyzer (SI 1287 and SI 1260). All catalyst coated electrodes underwent an activation process under the cyclic voltammetry (CV) mode, consisting of the voltage cycling range of 0.025–1 V vs. RHE, the cycling time of 50, the sweeping rate of 250 mV/sec, and the electrode rotation of 2500 rpm in oxygen-free electrolyte sufficiently purged by argon. After the activation process, the electrolyte was purged with oxygen for more than 10 mins and then, the ORR activities of the samples were measured by the linear sweeping voltammetry (LSV) mode, consisting of the voltage sweeping range of – 0.01–1.0 V vs. RHE, the sweeping rate of 20 mV/s, and the electrode rotation rate of 1600 rpm. LSV was performed several times to obtain a steady-state voltage-current curve and the polarization curve was measured for obtaining the limiting current density ( $i_l$ ), the kinetic current density ( $i_k$  at  $V = 0.9$  V vs. RHE), the specific current density ( $i_s$ ,  $i_k$  normalized by the roughness factor (RF)), and the mass activity ( $i_m$ ,  $i_k$  normalized by Pt loading). All aforementioned parameters indicating the ORR performance ( $i_k$ ,  $i_s$ , and  $i_m$ ) were achieved after correction considering i) the background LSV under Ar and ii) the electrolyte resistance by electrochemical impedance spectroscopy (EIS). After the ORR measurement, the electrolyte was re-saturated by argon and the activation process was performed again before obtaining the electrochemical active surface area (ECSA) measured by CV (voltage cycling range, 0.025–1.0 V; cycling time, 3; sweeping rate, 50 mV/s; electrode rotation rate, 0 rpm). The accelerated durability test (ADT) was measured by CV in an O<sub>2</sub>-saturated electrolyte (catalyst testing protocol, voltage cycling range, 0.6–1.0 V; cycling time, 10,000; sweeping rate, 100 mV/s; electrode rotation rate, 1600 rpm). After ADT, catalysts underwent the RDE testing protocol again in a new electrolyte. The ORR plots of Pt-Ti system show a mass transport limiting current density of 6.2–6.3 mA/cm<sup>2</sup>, which is within 10% of the theoretical mass transport limiting current, indicating that the catalyst coating on the electrode is of good quality and that the experimental measurement techniques are reliable [36].

## 2.3. Materials characterization

### 2.3.1. Compositional analyses, HRTEM, XPS, and SIMS

Platinum loadings on Pt/GC and Pt/TiO<sub>2</sub>/GC were quantified by an ICP mass spectroscopy (ICP-MS, Thermo Scientific, XSERIES 2). After removing platinum deposited on the sidewall and the back side of the GC disk, the electrode was immersed in aqua regia overnight to dissolve the platinum only deposited on the top of the electrode and then, the

platinum concentration in the aqua regia was measured. The morphology and diffraction pattern of the samples were confirmed by HRTEM image analysis using an aberration-corrected transmission electron microscope (FEI Titan ETEM 80-300) at 80 kV acceleration voltage. TEM grid with ultrathin carbon layer coated copper mesh (Ted Pella, 01824) was used for the substrate. Samples for HRTEM were prepared by the same processes as the Pt/TiO<sub>2</sub>/GC samples. XPS (PHI VersaProbe Scanning XPS Microscope) equipped with Al K $\alpha$  radiation of 1486 eV was used to measure the electron binding energies of Pt 4f and Ti 2p. The dynamic SIMS was carried out to investigate Pt, Ti, C, and O composition gradients at Evans Analytical Group (Sunnyvale, CA, USA): The depth and lateral resolutions are around 5 Å and 10 μm, respectively. Since the depth scale was not calibrated into the actual unit due to ultrathin nature of the samples, only qualitative depth profile information could be achieved from SIMS measurement. Due to surface roughening and having a platinum layer on top, there is some tailing of Pt into the underlying substrate. Note that the dynamic SIMS is appropriate for investigating the evolution of the near-surface structure of the Pt<sub>20</sub>/TiO<sub>2</sub>x15/GC catalysts with post H<sub>2</sub>-annealing since it has a higher depth resolution. ICP-based quantitative analyses on Ti leaching during the electrochemical testing were not successful since the amount of Ti in the aqueous electrolyte mainly originated from the Ti dissolution from Pt<sub>3</sub>Ti was negligible and below the detection limit. Specifically, if all Ti atoms (1.3 nmol) alloyed with Pt atoms (4 nmol) in the bulk Pt<sub>3</sub>Ti of Pt<sub>20</sub>/TiO<sub>2</sub>x15/GC are dissolved in 100 mL aqueous perchloric acid, which is the extreme case of Ti leaching from not only near surface layer, but also the bulk Pt<sub>3</sub>Ti, the resulting Ti concentration in the aqueous perchloric acid is calculated to be ca. 0.6 ppb, which is below the detection limit and also within the margin of error of ICP we used.

### 2.3.2. XAS studies

XAS measurements at the Pt L3 edge ( $\sim 11.56$  keV,  $k = 0\text{--}13$  Å<sup>−1</sup>), including both the extended X-ray absorption fine structure spectroscopy (EXAFS) and X-ray absorption near edge structure spectroscopy (XANES), were performed at the 11-2 beam line at the Stanford Synchrotron Radiation Lightsource (SSRL) at SLAC. XAS data were collected in the fluorescence mode with Zn mask as a filter and a 100-element Ge detector. During each sample scan, a Pt reference foil spectrum was simultaneously gathered. The data was first normalized in Athena software (Demeter, Version 0.9.26, Ref. [37]) by selecting appropriate points for the pre-edge and post-edge lines. The sample spectrum was shifted by aligning the reference that was gathered for the respective sample to Pt foil that had been calibrated.  $E_0$  for each sample spectrum was adjusted accordingly. The  $R$ -bkg was set to 1 Å. The spline range was set to be  $k$  of 0–13.3 Å<sup>−1</sup>. Each spectrum is actually the average of 2–3 EXAFS scans. Having merged, aligned and normalized the data, EXAFS data fittings were performed using Artemis software (Demeter, Version 0.9.26, Ref. [37]). Bulk Pt structure (crystallography open data (COD) number, 1011103) and cubic Pt<sub>3</sub>Ti (COD number, 1539263) were used to generate the interatomic scattering paths. These were imported to Artemis software where ATOMS was run, followed by FEFF simulations to generate all paths within 5 Å of absorbing center. A single shell model was used for the Pt foil and initially for all ALD samples. The  $k$  range for the forward Fourier transform was set to 3–12.5 Å<sup>−1</sup> and the back  $r$  range for the back Fourier transform was set to 1.7–3.15 Å. For the samples H<sub>2</sub> thermal-annealed up to 500 °C, the Pt single shell model worked well. However, a model for Pt<sub>3</sub>Ti was used to fit first shell Pt and Ti for other samples with H<sub>2</sub> thermal annealing above 500 °C. The same  $k$  and  $r$  range was used for these samples. The fits all showed misfits of < 1% and hence were regarded as probably accurate models for all cases.

## 2.4. Theory methods

### 2.4.1. DFT calculations

For DFT and strain calculations, all energies were calculated with the projector augmented-wave (PAW) method [38] implemented in the

GPW package [39] interfaced with Atomic Simulation Environment (ASE) with the Bayesian Error Estimation Functional with Van der Waals corrections (BEEF-vdW) exchange-correlation (XC) functional [40]. Built-in error estimation capabilities within the BEEF-vdW XC-functional creates an ensemble of functionals as well as an ensemble of energies, from which the predictive confidence of the calculation may be inferred. This error estimation capability has been previously used to describe uncertainty of predicting magnetic ground states [41], reaction mechanism pathways [42], heterogeneous catalysis [43], and solid-state physics [44]. Adsorbed O\* was calculated on a periodic  $2 \times 2$  unit cell 4 layers thick in a  $1/4$  monolayer coverage using a  $k$ -point mesh grid of  $6 \times 6 \times 1$ . Surface coverages of  $1/3$  monolayer OH\* and OOH\* on pure metals were modeled with an explicit water layer on a  $\sqrt{3} \times \sqrt{3}$  unit cell 4 layers deep with a  $6 \times 6 \times 1$   $k$ -point grid. Water stabilized OH\* and OOH\* on Pt<sub>3</sub>Ti(111) alloy based structures (bulk-terminated Pt<sub>3</sub>Ti,  $n \times \text{Pt/PtTi/Pt}_3\text{Ti}$ , and  $n \times \text{Pt/Pt}_3\text{Ti}$ , where  $n = 1, 2, 3$ ) were simulated using a  $2\sqrt{3} \times 2\sqrt{3}$  unit cell of at least 4 layers deep was used with a  $4 \times 4 \times 1$   $k$ -point grid. In all unit cells, the bottom two layers were fixed and at least a  $10 \text{ \AA}$  vacuum separation was used between unit cells. A real grid spacing of less than  $0.18 \text{ \AA}$  was used for all calculations. The structures were allowed to relax to a criterion of force less than  $0.05 \text{ eV/\AA}$ . Lattice constants of  $3.988 \text{ \AA}$  and  $4.022 \text{ \AA}$  were calculated for Pt<sub>3</sub>Ti and Pt, respectively. For hexagonal close packed surface of Ti in (0001) facet, the lattice constants were  $2.926 \text{ \AA}$  for  $a$  and  $4.733 \text{ \AA}$  for  $c$ .

#### 2.4.2. Strain calculations

To set a reference for the effect of compressive strain on adsorption characteristics on Pt(111), we calculate  $\Delta G_{\text{OH}^*}$  on a Pt(111) slab constructed from a lattice constant subject to 0–5% compressive strain at 1% intervals. At compressive strains greater than 5%, the surface tends to reconstruct. On a Pt(111) slab, a compressive strain of ca. 4–5% would most favorably weaken OH\* binding energy to the thermodynamically optimal (i.e., highest) limiting potential ( $U_L$ ) corresponding to the top of the volcano as shown in Fig. S12. However, the high strain would lead to a reduction in surface stability.

#### 2.4.3. DFT uncertainty calculations

Since the  $U_L$  values near the top of the volcano are numerically close to each other, confidence prediction metric was used to compare predicted performance of catalysts since the  $U_L$  values near the top of the volcano are numerically close to each other. In particular, due to inherent uncertainty within scaling relations of ORR intermediates, the  $U_L$  values at the weak binding leg of the volcano peak are strongly affected by the choice of the exchange-correlation (XC) functional within DFT [45]. The XC-functional BEEF-vdW, in addition to a best-fit functional, generates an ensemble of functionals spanning the single best-fit functional. An ensemble of energies is extracted from this ensemble of functionals. Agreement within the distribution of energy ensembles is used to derive the confidence of prediction for each calculation. Calculating the level of agreement between energies derived from the ensemble functionals and the best-fit functional a confidence value (c-value) metric is defined similar to what has been done in prior work [41]. Using  $G_{\text{OH}^*}$  as the descriptor, an interval confidence value ( $c_I$ ) describes the prediction certainty of a surface with an adsorption energy lying within an interval bounded by a left-limit, or a metal known to bind too strongly such as Pt(111), and a right-limit, or a metal known to bind too weakly such as Au(100), shown in Fig. S14. Au(100) is chosen as the right-limit since it has a similar activity to Pt(111). The following equation, Eq. (1), summarizes  $c_I$  for a surface  $S$  where  $N_{\text{ens}}$  is the number of functionals within the ensemble of functionals, and  $\Theta$  is the Heaviside function,

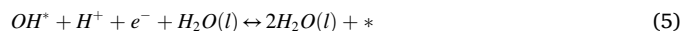
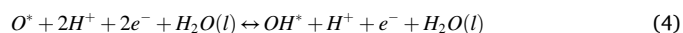
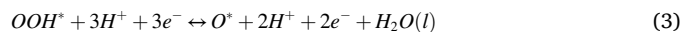
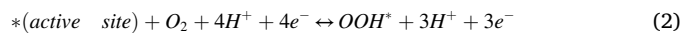
$$c_I = \frac{1}{N_{\text{ens}}} \left( \sum_{n=1}^{N_{\text{ens}}} \Theta(\Delta G_{S,n} - \Delta G_{\text{left-limit},n}) * \Theta(\Delta G_{\text{right-limit},n} - \Delta G_{S,n}) \right) \quad (1)$$

$c_I$  values calculated for all Pt-Ti alloy models with varying number of

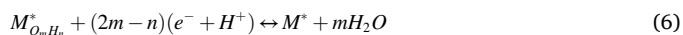
Pt overlayers ( $n \times \text{Pt/PtTi/Pt}_3\text{Ti}$ , and  $n \times \text{Pt/Pt}_3\text{Ti}$ , where  $n = 1, 2, 3$ ) are shown in Table S4.

#### 2.4.4. ORR mechanism calculations

We considered the 4-step oxygen reduction associative mechanism represented by Eqs. (2)–(5) in our computational study.



For an ORR adsorbate of the form of  $\text{O}_m\text{H}_n$  on a surface  $M$  with an active site  $*$ , a generalized reaction in reference to water is described in Eq. (6).



The change in free energy of adsorption is therefore defined in Eq. (7).

$$\Delta G_{\text{O}_m\text{H}_n} = G_{M^*_{\text{O}_m\text{H}_n}} - G_{M^*} - mG_{\text{H}_2\text{O}} + \left(m - \frac{n}{2}\right)G_{\text{H}_2} \quad (7)$$

where Gibbs free energy is calculated as adsorption energy corrected for entropy  $S$ , and zero point energy ZPE, in  $\Delta G = \Delta E_{\text{ref,water}} - T\Delta S + \Delta \text{ZPE}$ . These corrections and the corresponding adsorption energies calculated are described in Table S15 and Table S16, respectively.

### 3. Results and discussion

#### 3.1. ALD growth behaviors of TiO<sub>2</sub> on GC, Pt on GC, and Pt on TiO<sub>2</sub>-deposited GC

The deposition of TiO<sub>2</sub> and Pt by ALD was investigated on GC substrates. Fig. 1a demonstrates the ability to control the loading of Ti (deposited as TiO<sub>2</sub>) on GC through varying the number of ALD cycles. The deposition of Pt by ALD with  $N$  (number of) cycles on GC substrates with or without 15 cycles of TiO<sub>2</sub> ALD coating (Pt $\times$ N/GC and Pt $\times$ N/TiO<sub>2</sub> $\times$ 15/GC, respectively) was investigated, demonstrating a linear growth rate as a function of cycle number as shown in Fig. 1b. A benefit of using a thin TiO<sub>2</sub> underlayer for Pt ALD is the enhanced growth rate in comparison to bare GC (black squares in Fig. 1b) [33]. The morphology of the deposited Pt particles was further investigated by carrying out Pt ALD on the surface of ultrathin ( $\sim 3 \text{ nm}$ ) amorphous carbon-coated TEM grids preliminarily coated with TiO<sub>2</sub> by ALD. Fig. 1c displays HRTEM images showing the evolution of the Pt nanoparticle morphology with Pt ALD cycle number. Initially, distinct Pt nanoparticles were observed after 10 cycles (Pt $\times$ 10, Fig. 1c – left), with subsequent cycles resulting in interconnected particles forming branch-like structures (Pt $\times$ 15, Fig. 1c – center). Increasing the number of cycles to 20 (Pt $\times$ 20, Fig. 1c – right) leads to further horizontal nanoparticle expansion along with growth in the vertical direction that is indicated by the significant darkening of the deposited regions.

#### 3.2. ORR performance in terms of activity and stability

To induce the formation of Pt-Ti alloy from Pt deposited on TiO<sub>2</sub> layer, subsequent thermal annealing in H<sub>2</sub> was conducted at temperatures between 500 and 900 °C. The electrochemical activities of the resulting catalysts were evaluated by RDE testing in 0.1 M HClO<sub>4</sub> electrolyte at an electrode potential of 0.9 V vs. RHE, with ORR polarization and baseline CV plots provided in Figs. S1–S3. The effects of H<sub>2</sub> annealing temperature on the Pt-based mass activity towards the ORR is shown in Fig. 2a. A H<sub>2</sub> treatment temperature of 800 °C shows a maximum activity of  $1.84 \text{ A/mg}_{\text{Pt}}$ , a 2.8x enhancement in comparison to



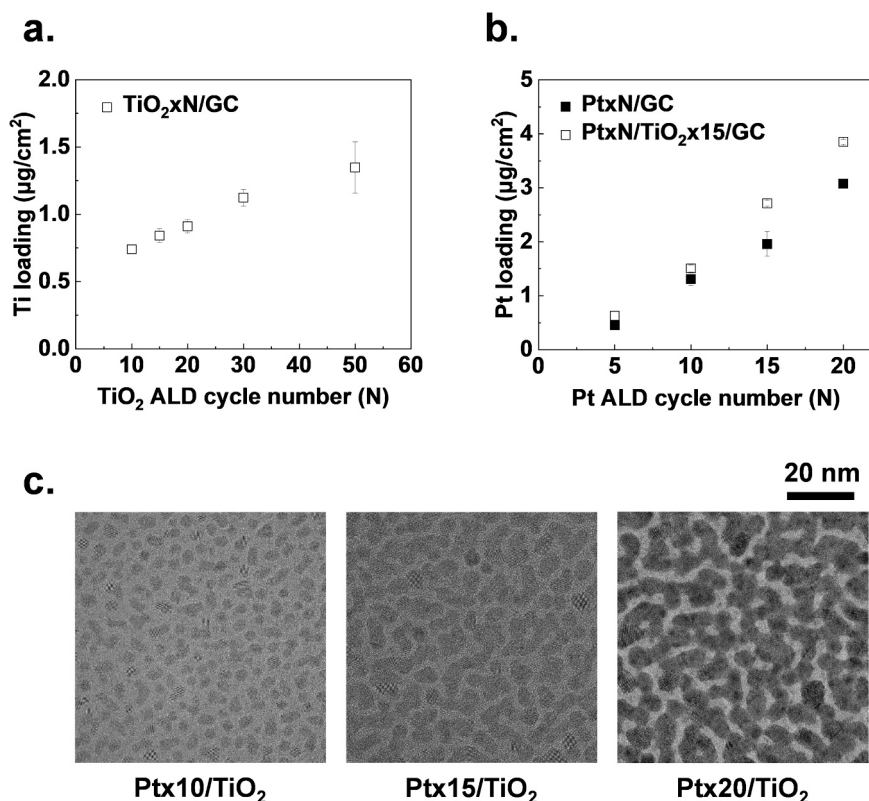


**Fig. 1.** Growth kinetics and characterization of  $\text{TiO}_2$  and Pt ALD. (a) Ti loading as a function of the number of  $\text{TiO}_2$  ALD cycles ( $N = 10, 15, 20, 30$ , and  $50$ ). (b) Pt loading as a function of the number of Pt ALD cycles ( $N = 5, 10, 15$ , and  $20$ ) for Pt deposition on GC and  $\text{TiO}_2 \times 15/\text{GC}$ . (c) Top-view bright-field HRTEM images of  $\text{Pt} \times N$  ( $N = 10, 15$ , and  $20$ ) deposited on  $\text{TiO}_2$ -coated amorphous carbon TEM grids.

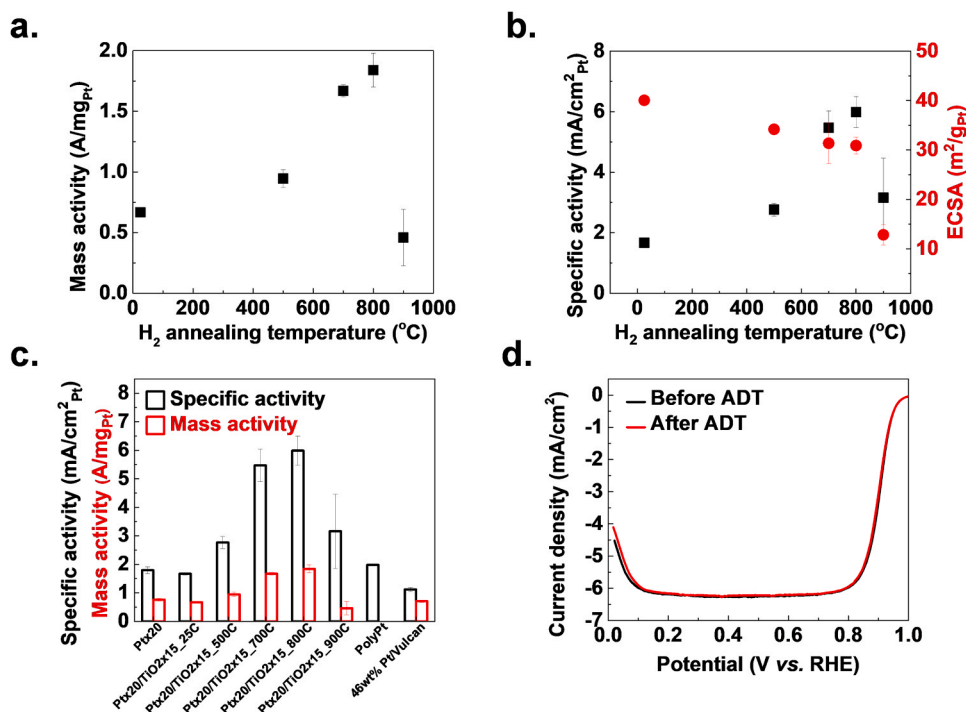


**Fig. 2.** ORR activity and stability of the as-developed  $\text{Pt}/\text{TiO}_2/\text{GC}$  and  $\text{Pt}/\text{GC}$  catalysts. Effects of thermal annealing of  $\text{Pt} \times 20/\text{TiO}_2 \times 15/\text{GC}$  in  $\text{H}_2$  at various temperatures on (a) Pt-based mass activities and (b) ECSAs and the specific activities at  $0.9 \text{ V}$  vs. RHE. Note that the cases of  $25^{\circ}\text{C}$  indicate as-deposited samples. (c) Summary of the specific activities and the Pt-based mass activities of i)  $\text{Pt} \times 20$ , ii)  $\text{Pt} \times 20/\text{TiO}_2 \times 15/\text{H}_2$ -treated at different annealing temperatures, iii) polycrystalline platinum, and iv) commercial  $\text{Pt}/\text{C}$  catalysts ( $46 \text{ wt}\% \text{ Pt/Vulcan}$  and  $46 \text{ wt}\% \text{ Pt/HSC}$ ). Note: The  $\text{Pt}/\text{C}$  data are taken from Ref. [46] where catalyst activities without the influence of Nafion were measured. (d) ORR polarization curves at  $1600 \text{ rpm}$  for  $\text{Pt} \times 20/\text{TiO}_2 \times 15/\text{GC}$  annealed under  $\text{H}_2$  at  $800^{\circ}\text{C}$  before and after ADT.

$\text{Pt} \times 20/\text{TiO}_2 \times 15/\text{GC}$  with no  $\text{H}_2$  treatment (denoted as  $25^{\circ}\text{C}$ ). Fig. 2b shows ECSAs ( $\text{m}^2/\text{g}_{\text{Pt}}$ ) determined by hydrogen underpotential deposition and the related specific activity as a function of  $\text{H}_2$  treatment temperature for the  $\text{Pt} \times 20/\text{TiO}_2 \times 15/\text{GC}$  catalysts. The ECSA decreases

gradually from  $40.0$  to  $30.9 \text{ m}^2/\text{g}_{\text{Pt}}$  with an increase in  $\text{H}_2$  treatment temperature up to  $800^{\circ}\text{C}$ , with a significant drop to  $12.8 \text{ m}^2/\text{g}_{\text{Pt}}$  observed upon further increasing the temperature to  $900^{\circ}\text{C}$ . The specific activity reaches a maximum of  $5.99 \text{ mA}/\text{cm}^2_{\text{Pt}}$  at  $0.9 \text{ V}$  vs. RHE for

the sample treated at a temperature of 800 °C (Fig. 2c), representing a more than 3-fold activity improvement over as-prepared Pt $\times$ 20/TiO $_2$  $\times$ 15/GC (1.66 mA/cm $^2_{Pt}$ ), along with Ti-free Pt $\times$ 20/GC (1.79 mA/cm $^2_{Pt}$ ) and a polycrystalline Pt electrode (Poly-Pt, 1.98 mA/cm $^2_{Pt}$ ) measured as references. This best performing catalyst (Pt $\times$ 20/TiO $_2$  $\times$ 15/GC annealed at 800 °C) also exhibits the best Pt mass-based activity that was more than 2-fold higher than commercial Vulcan carbon black supported Pt (46 wt% Pt/Vucan). To probe the electrochemical stability of the Pt $\times$ 20/TiO $_2$  $\times$ 15/GC catalyst treated at 800 °C in H $_2$ , an ADT consisting of 10,000 electrode potential cycles between 0.6 and 1.0 V vs RHE in O $_2$  saturated 0.1 M HClO $_4$  was performed. The catalyst maintained its excellent ORR activity through this process, with almost identical ORR activities (Fig. 2d) and ECSA values (Fig. S3) determined before and after ADT. For comparison, the commercial Pt/C catalyst (46 wt% Pt/high-surface-carbon (HSC) catalyst, Kikinzoku Kogyo K. K.) exhibited significant losses of kinetic current density and ECA of 21% and 14%, respectively under the same ADT protocol [25].

### 3.3. Materials characterization based on microscopic and spectroscopic techniques

To gain insight underlying the significant ORR activity enhancement observed following thermal annealing in H $_2$ , the catalysts were characterized by various microscopic and spectroscopic techniques. The effects of H $_2$  annealing temperature on morphology are depicted in Fig. 3a, showing the HRTEM images of Pt $\times$ 20/TiO $_2$  $\times$ 15 deposited on

amorphous carbon coated TEM grids, which we previously demonstrated to have a similar surface chemistry to that of GC substrates, albeit with less surface roughness (RMS roughness of ca. 1 Å for the carbon coated TEM grids and ca. 19 Å for GC) [25]. The thermal annealing in H $_2$  induces morphological changes, whereby the platinum nanoparticles show gradual coalescence up to 700 °C in the form of a branched morphology. Increasing the heat treatment temperature from 700 to 800 °C induces more significant Pt agglomeration into particles with diameters larger than  $\sim$ 10 nm. Interestingly, the trends from electrochemical characterization indicate only a very minor decrease in ECSA with this H $_2$  annealing temperature increase (Fig. 2b), not necessarily expected given the significant particle agglomeration observed by HRTEM. We speculate this arises due to the aforementioned differences in the surface roughness for GC (RMS roughness  $\sim$ 19 Å) versus the carbon coated TEM grids (1 Å). The significantly higher surface roughness of GC increases the average path length for particle migration, thereby likely suppressing significant particle agglomeration until slightly higher temperature. This hypothesis is consistent with the dramatic reduction in ECSA observed going from a H $_2$  thermal annealing temperature of 800–900 °C (Fig. 2b). XPS was further conducted to understand the evolution of chemical states of Pt/TiO $_2$  $\times$ 15/GC after H $_2$  thermal treatment, with clear changes in the electronic structures of Pt and Ti observed in the spectra (Fig. 3b). For metallic Pt, the shift in the Pt4f $_{7/2}$  peak observed with the increase in H $_2$  annealing temperature above 500 °C suggests the formation of Pt-Ti bonds within the catalyst [34,47]. For Ti 2p $_{3/2}$  spectra, although the majority of Ti is present in 4+

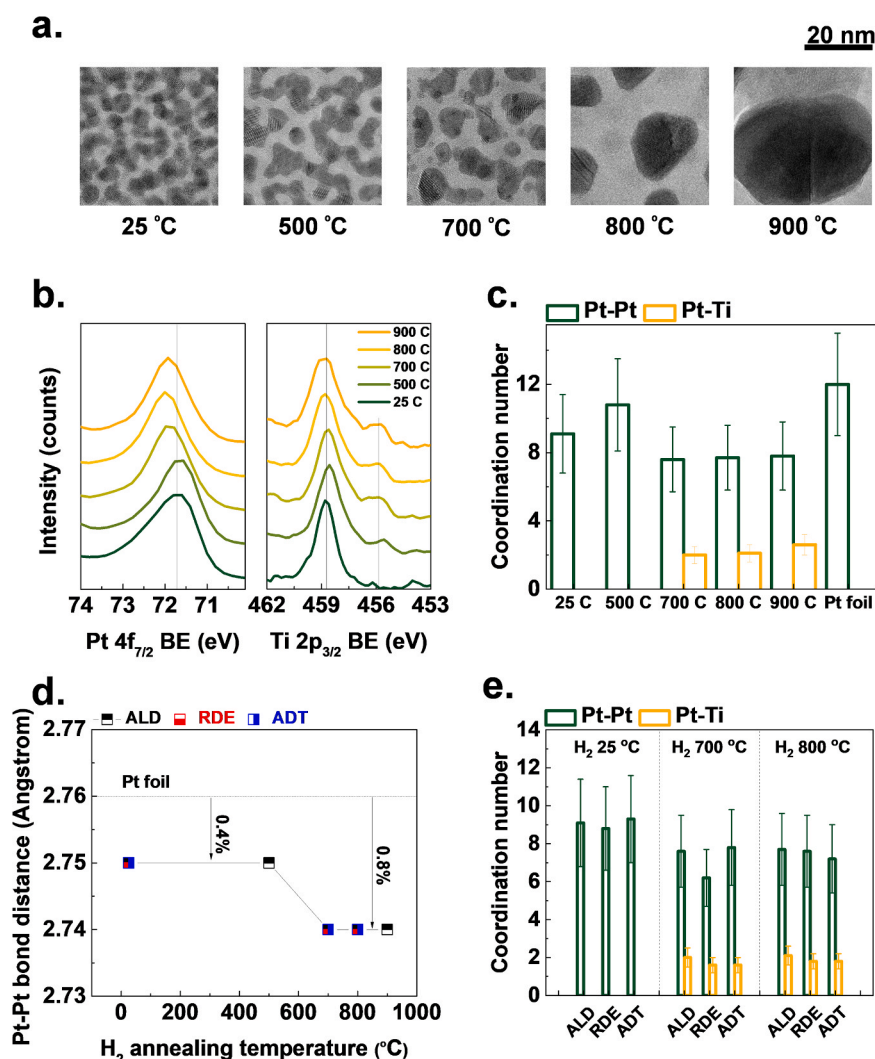


**Fig. 3.** Materials characterization of the as-developed Pt/TiO $_2$ /GC catalysts. (a) Top-view bright-field HRTEM images of Pt $\times$ 20/TiO $_2$  $\times$ 15/GC as a function of H $_2$  annealing temperature (25–900 °C). Note that the case of 25 °C is the as-deposited sample. (b) Pt4f $_{7/2}$  and Ti2p $_{3/2}$  XPS spectra of Pt/TiO $_2$  $\times$ 15/GC with respect to H $_2$  annealing temperatures (25–900 °C) before the electrochemical testing. (c–e) XAS results showing coordination numbers (CNs) and Pt–Pt bond distances (R $_{Pt-Pt}$ ), including the evolution of (c) CNs of Pt–Pt and Pt–Ti and (d) Pt–Pt bond distance (R $_{Pt-Pt}$ ) for Pt $\times$ 20/TiO $_2$  $\times$ 15/GC with respect to H $_2$  annealing temperature as well as the evolution of (d) R $_{Pt-Pt}$  and (e) CNs of Pt–Pt and Pt–Ti of Pt $\times$ 20/TiO $_2$  $\times$ 15/GC treated at different annealing temperatures (as deposited, 700, and 800 °C) after initial activity measurement (RDE) and 10,000 cycle durability test (ADT). CNs of the as-deposited sample are labeled as ALD. The collected XAS spectra, which were used to generate the plots and calculate the values shown in Fig. 3c–e, are all provided in the Supporting information in Fig. S6, S7, S8, S9 and Table S3.

state (peak at  $\sim 459$  eV), a peak around 455.5 eV emerges, consistent with metallic Ti found in a Pt-Ti alloy (a list of XPS binding energy values of Pt  $4f_{7/2}$  and Ti  $2p_{3/2}$  in different oxidation states is presented in Table S1).

### 3.4. XAS studies

To more rigorously probe the formation of the Pt-Ti alloy resulting from thermal annealing in  $H_2$ , Pt L3 XAS characterization of the catalyst materials was conducted. EXAFS fittings were conducted to determine the average CNs of the Pt atoms in Pt $\times 20$ /TiO $_2 \times 15$ /GC samples with different annealing temperatures, as shown in Fig. 3c. For Pt $\times 20$ /TiO $_2 \times 15$ /GC, the as-prepared sample and the sample annealed in  $H_2$  at 500 °C shows no Pt-Ti coordination, indicating these species are mostly still present as two distinct phases (Pt and TiO $_x$ ) in the catalyst materials. The formation of Pt-Ti coordination is confirmed for samples  $H_2$ -annealed at or above 700 °C, and the ratios of the Pt-Pt CN ( $CN_{Pt-Pt}$ ) to Pt-Ti CN ( $CN_{Pt-Ti}$ ) of those samples are 3.8, 3.7, and 3.0 at 700, 800, and 900 °C, respectively. The decrease in the ratios at higher temperatures could be explained by an increase in the formation of Pt $_3$ Ti due to greater intermixing of Pt and TiO $_x$ . Fast Fourier transform (FFT) diffraction patterns of the catalysts annealed at different temperatures in  $H_2$  also indicates the formation of the Pt $_3$ Ti alloy structure at annealing temperatures above 700 °C (Fig. S4). Pt–Pt bond distances ( $R_{Pt-Pt}$ ) determined through EXAFS fitting are shown in Fig. 3d. The reference Pt foil showed a ( $R_{Pt-Pt}$ ) of 2.76 Å. The  $R_{Pt-Pt}$  values of all as-deposited ALD-based catalysts were 2.75 Å, representing a 0.4% contraction versus the Pt-foil, which is a common observation for nanoparticles [48].  $H_2$  annealing up to 500 °C does not induce any changes in the  $R_{Pt-Pt}$  for Pt $\times 20$ /TiO $_2 \times 15$ /GC, however thermal annealing in  $H_2$  beyond 500 °C causes further contraction in the Pt–Pt bond distance, ca. 0.8% contraction versus the Pt-foil reference. The electrochemical stability of these Pt-Ti alloys was also probed by EXAFS analysis of the Pt $\times 20$ /TiO $_2 \times 15$ /GC, revealing minimal changes in the  $CN_{Pt-Pt}$  and  $CN_{Pt-Ti}$  (Fig. 3e) and  $R_{Pt-Pt}$  (Fig. 3d) values observed after the initial ORR activity measurement (denoted RDE) and following ADT, indicating that the bulk Pt-Ti alloys are electrochemically stable under the conditions investigated. We further found out that un-alloyed TiO $_2$  during the  $H_2$  annealing step was crystallized to different TiO $_2$  phases (Fig. S5). The formation of rutile, brookite, and anatase TiO $_2$  phases was confirmed from the Pt $\times 20$ /TiO $_2 \times 15$ /GC catalysts  $H_2$ -annealed at 700 °C and 800 °C.

### 3.5. SIMS and DFT results: surface reconstruction of the Pt $_3$ Ti alloy

It has been well-established that the ORR enhancement of Pt-based bimetallic electrocatalysts commonly arises from the formation of a Pt overlayer structure with modulated electronic and geometric structure induced from the underlying alloy [3,5] although this understanding has been primarily linked to Pt-Co or Pt-Ni catalysts that are intrinsically prone to base metal dissolution, or to Pt-lanthanide alloy catalysts that are difficult to prepare in nanoparticle form. Generally speaking, the composition of the near-surface layer plays a significant role on oxygen adsorption energies and, by extension, the catalytic activity [4]. As such, we postulate that surface reconstruction of the Pt $_3$ Ti alloy catalysts occurred during electrochemical testing, based on the observation of a steady increase in ORR activity as a function of the number of cycles of electrochemical activation in O $_2$ -saturated 0.1 M HClO $_4$  electrolyte by LSV. For the Pt $\times 20$ /TiO $_2 \times 15$ /GC catalyst annealed in  $H_2$  at 800 °C, we activated the catalyst by cycling the electrode potential between  $-0.01$ – $1$  V vs. RHE (Fig. S11). Continuous increases in activity were observed up to 30 activation cycles, after which stable ORR polarization curves were obtained. Conversely, the pure Pt catalyst (Pt $\times 20$ ) showed relatively minimal activity improvements as a function of cycle number and stable polarization curves observed after approximately only ten activation cycles. To probe the near surface compositions, we performed

dynamic SIMS analyses to investigate the compositional gradients of Pt and Ti in these samples before and after electrochemical testing (Fig. 4a). For the near-surface region, platinum enrichment was clearly observed after electrochemical testing (both RDE and ADT) compared to the as-prepared sample (labelled ALD). However, the bulk compositional depth profiles were similar for the three samples indicating that electrochemical processes predominantly induced changes near the surface, and that the bulk alloy structures of these materials ideally possess high stability even after extensive ADT; stability trends that are consistent with thermodynamic calculations reported previously [4].

With this structural insight, we perform DFT calculations to explore possible mechanisms underlying the enhanced ORR activity observed. As previously suggested by Greeley et al. [4], two Pt-Ti alloy catalysts were modeled through different Pt overlayer formation mechanisms (leaching vs. exchanging), where the topmost Ti-containing layer is either 50% Ti (Pt/PtTi/Pt $_3$ Ti) or 25% Ti (Pt/Pt $_2$ Ti) (Fig. 4b), respectively. Both models were considered with  $n$  number of Pt overlayers, where  $n$  is 1, 2, or 3. Assuming that the Pt overlayer is thinner than the Pt $_3$ Ti alloy layers such that the strain of the bulk dominates relative to a pure Pt(111) surface, we predict 0.85% compressive strain induced on overlaying Pt slabs for both models. This value is very close to the experimentally observed strain of  $\sim 0.8\%$  determined by EXAFS fitting on Pt $\times 20$ /TiO $_2 \times 15$ /GC  $H_2$ -annealed above 700 °C (Fig. 3d). Such strain is predicted to weaken the OH\* binding energy by only 0.04 eV as shown in Fig. S12 (Volcano plot of pure platinum at different strains) suggesting that further increases in the limiting potential are due to ligand effects of the underlying alloy. We compute adsorption energies of three ORR intermediates, O\*, OH\*, and OOH\*, on Pt $_3$ Ti(111) alloy based structures (Table S4) and compare our findings to unstrained Pt(111). The free energy diagram at a potential of 0.9 V vs. RHE (Fig. 4c) compares the thermodynamic free energy landscape of both Pt-Ti model surfaces with Pt(111). The surfaces with the thinnest Pt overlayer ( $n = 1$ ) provide the largest modulation in adsorption strengths of oxygen intermediates. The limiting step on 1xPt/PtTi/Pt $_3$ Ti is calculated to be the activation of O $_2$  into OOH\* (first ORR elementary step,  $O_2 + 4H^+ + 4e^- \rightarrow OOH* + 3H^+ + 3e^-$ ), and on 1xPt/Pt $_2$ Ti is calculated to be the desorption of OH\* (last ORR elementary step,  $OH* + H^+ + e^- + H_2O(l) \rightarrow 2H_2O(l)$ ). We find that the limiting potential and step could be modulated through the proximity of Ti atoms in the subsurface layer that can weaken the adsorption energetics of oxygen intermediates with the surface Pt layer. ORR performance was evaluated by the calculated limiting potential, or the highest potential where all reaction steps become exergonic, as a function of the change in free energy of OH\*,  $\Delta G_{OH^*}$ . The free energy of the OH\* intermediate is used as the descriptor since it leads to the highest prediction robustness for the ORR [45]. Theoretical  $U_L$  values for Pt(111) and Pt-Ti alloys are shown on an activity volcano following the Sabatier principle in Fig. 4d. We calculate that Pt(111) overbinds oxygen, leading to less optimal ORR energetics by a difference of  $\sim 0.2$  eV from the scaling-limited maximum limiting potential [49]. Relative to a pure Pt(111) slab, both  $n = 1$  and 2 overlayers of Pt on models  $nx$ Pt/PtTi/Pt $_3$ Ti and  $nx$ Pt/Pt $_2$ Ti are calculated to have a weaker OH\* binding energy by 0.11–0.23 eV and therefore a higher theoretical  $U_L$ . The weakening of oxygen binding energies on Pt metal with a Pt-Ti alloy subsurface composition is consistent with prior calculations in the literature [50]. However, near the top of the volcano distinguishability of  $U_L$  between surfaces is the lowest due to propagation of uncertainty throughout the thermodynamic model [45]. This makes it difficult to predict whether a surface is energetically better than Pt(111) with a high degree of certainty in DFT. The exchange-correlation Bayesian Error Estimation Functional with Van der Waal corrections (BEEF-vdW) is used for the built-in uncertainty quantification capability within DFT. The level of agreement between energies generated by BEEF-vdW is defined as an interval confidence value ( $c_f$ ) for calculating whether the adsorption energy on a surface lies in the interval between strongly and weakly binding reference surfaces (Table S4). Based on this analysis, we find that there is 99% confidence



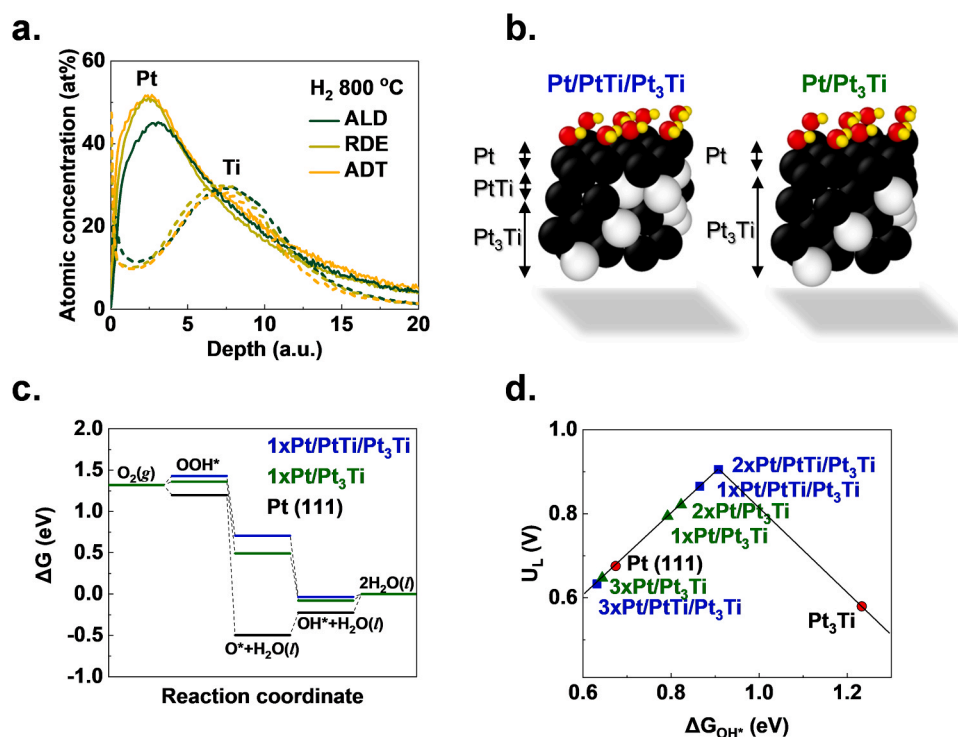


**Fig. 4.** SIMS study and DFT simulation for the best-performing Pt-Ti alloy catalysts. (a) SIMS-measured atomic concentration evolution of Pt (solid) and Ti (dotted) with respect to sputter depth (C and O profiles are not shown in this figure, for simplicity, but shown in Fig. S10 along with Ti and Pt). (b) Two possible models, Pt/PtTi/Pt<sub>3</sub>Ti and Pt/Pt<sub>3</sub>Ti, examined in this study by DFT for evaluating ORR activity. (c) Calculated free energy diagram for ORR at a potential of 0.9 V vs. RHE for Pt(111) (black), 1×Pt/PtTi/Pt<sub>3</sub>Ti (blue), and 1×Pt/Pt<sub>3</sub>Ti (green). (d) Volcano relationship plot of ORR activities represented by  $U_L$  vs. OH binding energies with water stabilization ( $\Delta G_{OH^*}$ ) calculated by DFT for different alloy models in (111) crystal lattice (bulk-terminated Pt<sub>3</sub>Ti,  $n \times$  Pt/PtTi/Pt<sub>3</sub>Ti, and  $n \times$  Pt/Pt<sub>3</sub>Ti, where  $n = 1, 2, 3$ ). On bulk-terminated Pt<sub>3</sub>Ti surface, OH\* binding energy is calculated on the Pt site without explicit water molecules.

that OH\* adsorption on 1xPt/PtTi/Pt<sub>3</sub>Ti and 1xPt/Pt<sub>3</sub>Ti is between the adsorption energies that correspond to relatively strong binding Pt(111) and relatively weak binding Au(100) surfaces. Au(100) was chosen as the weak-binding reference because it is predicted to have a similar  $U_L$  as Pt(111) (Fig. S13). This gives high degree of confidence that  $U_L$  of such Pt-Ti alloy surfaces would surpass both reference metals. Since the observed strain is predicted to weaken OH\* by < 0.1 eV, improvement in the ORR performance observed both experimentally and computationally suggests that strain effects are not purely responsible. Generally, the OH\* binding energy of both models approaches that of pure Pt(111) as ligand effects of the underlying alloy weaken through a thicker Pt layer. Computational analyses indicate a promising approach to prepare highly active catalysts is to prepare overlayer structures with a low number of Pt layers. Increases in activity observed experimentally, therefore, may be rationalized by both ligand effect of underlying titanium lattice at thinner Pt overlayers and strain effects dominating at thicker Pt overlayers.

#### 4. Conclusion

ALD with atomic level control of both Pt and Ti loadings along with the superior wettability of Pt ALD precursors onto TiO<sub>2</sub> allowed us to leverage SMSIs occurring between these two species that led to the formation of Pt<sub>3</sub>Ti alloys during the thermal annealing in H<sub>2</sub>. The catalyst H<sub>2</sub>-annealed at 800 °C showed a Pt-based mass activity of 1.84 mA/g<sub>Pt</sub> at 0.9 V vs. RHE, representing more than 2-fold improvement in ORR activity in comparison to pure Pt nanoparticles prepared by ALD and commercial Pt/Vulcan catalyst. Intrinsic activity improvements were indicated by the 3-fold higher specific activity for the optimized ALD prepared Pt<sub>3</sub>Ti catalyst compared to a polycrystalline Pt electrode. Combined XPS, EXAFS, HRTEM, and SIMS characterization indicated the catalyst was comprised of a Pt<sub>3</sub>Ti alloy with a Pt enriched surface. By correlating experimental observations with DFT calculations, we developed new insight into the ORR activity of Pt<sub>3</sub>Ti catalysts that arises due to a combination of strain and ligand effects. Additionally, the activity of Pt<sub>3</sub>Ti catalysts was retained following 10,000 ADT cycles, attributed to the intrinsic stability of the bulk Pt<sub>3</sub>Ti phase and

supported by near-negligible amounts of Ti dissolution observed experimentally following electrochemical testing. Of note, we have used RDE to experimentally quantify the intrinsic activity and stability capabilities of ALD prepared Pt<sub>3</sub>Ti catalysts. Many past catalyst configurations introduced in Table S7 rely on Pt alloying with metals (i.e., Ni) that are intrinsically unstable under fuel cell conditions and can leach out, impacting the performance of the catalyst, along with the ionomer and electrolyte membrane. Also, other past Pt-lanthanide catalytic configurations rely on difficult to formulate alloys that are difficult to translate to nanoparticulate form. This has also been a challenge with Pt-Ti, but we have overcome this with our ALD/annealing approach. Our good stability results supported by theory [4], and thus we hope it encourages the field to more carefully consider Pt-Ti as an option. We recognize that good RDE results do not always translate to good fuel cell performance. Membrane electrode assembly (MEA) integration of these catalysts is currently ongoing but is outside the scope of the present work and will be featured in other publications. Nevertheless, the high performance of the ALD-prepared Pt<sub>3</sub>Ti catalysts and fundamental insight into the performance-structure-property relationships can guide the development of advanced high activity and stability catalysts, which will be essential parts of the next-generation MEA. Once our findings of ALD-prepared Pt-Ti catalysts on bulk carbon RDE disks will be transferred to more practical carbon (e.g. Vulcan and HSC carbon) supported nanoparticle structures that do not require destructive TEM sample preparation, STEM imaging along with atomic scale elemental mapping based on either EELS or EDX could provide more insight into this catalyst system, especially if this material characterization is coupled with electrochemical testing of the powder samples.

#### CRedit authorship contribution statement

**Yongmin Kim:** Conceptualization, Investigation, Writing – original draft. **Shicheng Xu:** Investigation (ALD). **Joonsuk Park:** Investigation (TEM). **Anup Lal Dadlani:** Investigation (XAFS). **Olga Vinogradov:** Investigation (DFT). **Dilip Krishnamurthy:** Investigation (DFT). **Marat Orazov:** Investigation (Electrochemistry). **Dong Un Lee:** Investigation (Electrochemistry). **Sam Dull:** Investigation (Electrochemistry). **Peter**



**Schindler:** Investigation (TEM). **Hyun Soo Han:** Investigation (Electrochemistry). **Zhaoxuan Wang:** Investigation (ALD). **Tanja Graf:** Resources. **Thomas D. Schladt:** Resources. **Jonathan E. Mueller:** Data analyses (DFT). **Ritimukta Sarangi:** Data analyses (XAFS). **Ryan Davis:** Investigation (XAFS). **Venkatashubramanian Viswanathan:** Supervision of simulation works. **Thomas Francisco Jaramillo:** Funding acquisition, Writing – review & editing. **Drew C. Higgins:** Supervision of experimental works, Writing – review & editing. **Fritz B. Prinz:** Project administration, Funding acquisition, Writing – review & editing.

## Declaration of Competing Interest

The authors declare that they have no known competing financial interests or personal relationships that could have appeared to influence the work reported in this paper.

## Acknowledgement

This work was supported financially by the Volkswagen Group of America. Part of this work was performed at the Stanford Nano Shared Facilities (SNSF), supported by the National Science Foundation under award ECCS-1542152. Y. K. thanks support from and discussions with Kipil Lim, Alexey Boubnov, and Chuck Hitzman. D.H. acknowledges support from the Banting Postdoctoral Fellowship, administered by the government of Canada. P.S. acknowledges financial support from the Austrian Science Fund (FWF) under contract J3980-N27. A.L.D. was funded by the Norwegian Research Council under project number 274459 Trånslate.

## Appendix A. Supporting information

Supplementary data associated with this article can be found in the online version at [doi:10.1016/j.apcatb.2021.120741](https://doi.org/10.1016/j.apcatb.2021.120741).

## References

- [1] D. Papageorgopoulos, U. Department of Energy, Fuel Cells Sub-Program Overview; DOE Hydrogen and Fuel Cells Program FY 2017 Annual Progress Report, 2017.
- [2] N. Cheng, L. Zhang, K. Doyle-Davis, X. Sun, Single-atom catalysts: from design to application, *Electrochem. Energy Rev.* 2 (24) (2019) 539–573, <https://doi.org/10.1007/S41918-019-00050-6>.
- [3] V.R. Stamenkovic, B.S. Mun, M. Arenz, K.J.J. Mayrhofer, C.A. Lucas, G. Wang, P. N. Ross, N.M. Markovic, Trends in electrocatalysis on extended and nanoscale Pt-bimetallic alloy surfaces, *Nat. Mater.* 6 (2007) 241–247, <https://doi.org/10.1038/nmat1840>.
- [4] J. Greeley, I.E.L. Stephens, A.S. Bondarenko, T.P. Johansson, H.A. Hansen, T. F. Jaramillo, J. Rossmeisl, I. Chorkendorff, J.K. Nørskov, Alloys of platinum and early transition metals as oxygen reduction electrocatalysts, *Nat. Chem.* 1 (2009) 552–556, <https://doi.org/10.1038/nchem.367>.
- [5] M. Escudero-Escribano, P. Malacrida, M.H. Hansen, U.G. Vej-Hansen, A. Velázquez-Palenzuela, V. Tripkovic, J. Schiøtz, J. Rossmeisl, I.E.L. Stephens, I. Chorkendorff, Tuning the activity of Pt alloy electrocatalysts by means of the lanthanide contraction, *Science* 352 (2016) 73–76, <https://doi.org/10.1126/science.aad8892>.
- [6] R. Wu, P. Tsiakaras, P.K. Shen, Facile synthesis of bimetallic Pt-Pd symmetry-broken concave nanocubes and their enhanced activity toward oxygen reduction reaction, *Appl. Catal. B: Environ.* 251 (2019) 49–56, <https://doi.org/10.1016/j.apcatb.2019.03.045>.
- [7] D. Dang, L. Zhang, X. Zeng, X. Tian, C. Qu, H. Nan, T. Shu, S. Hou, L. Yang, J. Zeng, S. Liao, In situ construction of Ir@Pt/C nanoparticles in the cathode layer of membrane electrode assemblies with ultra-low Pt loading and high Pt exposure, *J. Power Sources* 355 (2017) 83–89, <https://doi.org/10.1016/j.jpowsour.2017.04.050>.
- [8] Kieran Doyle-Davis Lei Zhang, Xueliang Sun, Pt-Based electrocatalysts with high atom utilization efficiency: from nanostructures to single atoms, *Energy Environ. Sci.* 12 (2019) 492–517, <https://doi.org/10.1039/C8EE02939C>.
- [9] Y. Liu, W.E. Mustain, High stability, high activity Pt/ITO oxygen reduction electrocatalysts, *J. Am. Chem. Soc.* 135 (2013) 530–533, <https://doi.org/10.1021/ja307635r>.
- [10] Q. Jia, S. Ghoshal, J. Li, W. Liang, G. Meng, H. Che, S. Zhang, Z.F. Ma, S. Mukerjee, Metal and metal oxide interactions and their catalytic consequences for oxygen reduction reaction, *J. Am. Chem. Soc.* 139 (2017) 7893–7903, <https://doi.org/10.1021/jacs.7b02378>.
- [11] W.W. McNear, A.E. Linico, C. Ngo, S. van Rooij, S. Haussener, M.E. Maguire, S. Pylypenko, A.W. Weimer, Atomic layer deposition of TiO<sub>2</sub> for stabilization of Pt nanoparticle oxygen reduction reaction catalysts, *J. Appl. Electrochem.* 48 (2018) 973–984, <https://doi.org/10.1007/s10800-018-1226-y>.
- [12] C. Park, E. Lee, G. Lee, Y. Tak, Superior durability and stability of Pt electrocatalyst on N-doped graphene-TiO<sub>2</sub> hybrid material for oxygen reduction reaction and polymer electrolyte membrane fuel cells, *Appl. Catal. B: Environ.* 268 (2020), 118414, <https://doi.org/10.1016/j.apcatb.2019.118414>.
- [13] L. J. T. H. T. X. H. S. L. X. D. L. L. S. Highly selective TiN-supported highly dispersed Pt catalyst: ultra active toward hydrogen oxidation and inactive toward oxygen reduction, *ACS Appl. Mater. Interfaces* 10 (2018) 3530–3537, <https://doi.org/10.1021/ACSAMI.7B15159>.
- [14] E. Antolini, J.R.C. Salgado, E.R. Gonzalez, The stability of Pt–M (M = first row transition metal) alloy catalysts and its effect on the activity in low temperature fuel cells: a literature review and tests on a Pt–Co catalyst, *J. Power Sources* 160 (2006) 957–968, <https://doi.org/10.1016/j.jpowsour.2006.03.006>.
- [15] C. Roy, B.P. Knudsen, C.M. Pedersen, A. Velázquez-Palenzuela, L.H. Christensen, C.D. Damsgaard, I.E.L. Stephens, I. Chorkendorff, Scalable Synthesis of Carbon-Supported Platinum-Lanthanide and -Rare-Earth Alloys for Oxygen Reduction, 2018, (<https://doi.org/10.1021/acscatal.7b03972>).
- [16] J. Choi, J. Cho, C.W. Roh, B.S. Kim, M.S. Choi, H. Jeong, H.C. Ham, H. Lee, Au-doped PtCo/C catalyst preventing Co leaching for proton exchange membrane fuel cells, *Appl. Catal. B: Environ.* 247 (2019) 142–149, <https://doi.org/10.1016/j.apcatb.2019.02.002>.
- [17] X. Peng, S. Zhao, T.J. Omasta, J.M. Roller, W.E. Mustain, Activity and durability of Pt–Ni nanocage electrocatalysts in proton exchange membrane fuel cells, *Appl. Catal. B: Environ.* 203 (2017) 927–935, <https://doi.org/10.1016/j.apcatb.2016.10.081>.
- [18] D. P. CRC handbook of chemistry and physics, *J. Mol. Struct.* (1992), [https://doi.org/10.1016/0022-2860\(92\)85083-S](https://doi.org/10.1016/0022-2860(92)85083-S).
- [19] L. Li, F. Abild-Pedersen, J. Greeley, J.K. Nørskov, Surface tension effects on the reactivity of metal nanoparticles, *J. Phys. Chem. Lett.* 6 (2015) 3797–3801, <https://doi.org/10.1021/acs.jpclett.5b01746>.
- [20] A. Jackson, V. Viswanathan, A.J. Forman, A.H. Larsen, J.K. Nørskov, T. F. Jaramillo, Climbing the activity volcano: core-shell Ru@Pt electrocatalysts for oxygen reduction, *ChemElectroChem* 1 (2014) 67–71, <https://doi.org/10.1002/celec.201300117>.
- [21] A.L. Strickler, A. Jackson, T.F. Jaramillo, Active and stable Ir@Pt core-shell catalysts for electrochemical oxygen reduction, *ACS Energy Lett.* 2 (2017) 244–249, <https://doi.org/10.1021/acseenergylett.6b00585>.
- [22] A. Jackson, A. Strickler, D. Higgins, T. Jaramillo, A. Jackson, A. Strickler, D. Higgins, T.F. Jaramillo, Engineering Ru@Pt core-shell catalysts for enhanced electrochemical oxygen reduction mass activity and stability, *Nanomaterials* 8 (2018) 38, <https://doi.org/10.3390/nano8010038>.
- [23] D.C. Harris, Quantitative Chemical Analysis, W.H. Freeman and Co, 2007.
- [24] J. Kim, S. Yang, H. Lee, Platinum–titanium intermetallic nanoparticle catalysts for oxygen reduction reaction with enhanced activity and durability, *Electrochem. Commun.* 66 (2016) 66–70, <https://doi.org/10.1016/j.elecom.2016.03.007>.
- [25] S. Xu, Y. Kim, J. Park, D. Higgins, S.J. Shen, P. Schindler, D. Tian, J. Provine, J. Torgersen, T. Graf, T.D. Schladt, M. Orazov, B.H. Liu, T.F. Jaramillo, F.B. Prinz, Extending the limits of Pt/C catalysts with passivation-gas-incorporated atomic layer deposition, *Nat. Catal.* 1 (2018) 624–630, <https://doi.org/10.1038/s41929-018-0118-1>.
- [26] Q. Hu, S. Wang, Z. Gao, Y. Li, Q. Zhang, Q. Xiang, Y. Qin, The precise decoration of Pt nanoparticles with Fe oxide by atomic layer deposition for the selective hydrogenation of cinnamaldehyde, *Appl. Catal. B: Environ.* 218 (2017) 591–599, <https://doi.org/10.1016/j.apcatb.2017.06.087>.
- [27] J. Zhang, W. Chen, H. Ge, C. Chen, W. Yan, Z. Gao, J. Gan, B. Zhang, X. Duan, Y. Qin, Synergistic effects in atomic-layer-deposited PtCo/CNTs catalysts enhancing hydrolytic dehydrogenation of ammonia borane, *Appl. Catal. B Environ.* 235 (2018) 256–263, <https://doi.org/10.1016/j.apcatb.2018.04.070>.
- [28] B. Wang, Y.T. Chen, T.Y. Chang, Z. Jiang, Z.Q. Huang, S.Y. Wang, C.R. Chang, Y. S. Chen, J.J. Wei, S. Yang, T. Fang, Facet-dependent catalytic activities of Pd/rGO: exploring dehydrogenation mechanism of dodecahydro-N-ethylcarbazole, *Appl. Catal. B: Environ.* 266 (2020), 118658, <https://doi.org/10.1016/j.apcatb.2020.118658>.
- [29] J. Han, Y. Kim, D.H.K. Jackson, H. Chang, H.W. Kim, J. Lee, J.R. Kim, Y. Noh, W. B. Kim, K.Y. Lee, H.J. Kim, Enhanced catalytic performance and changed reaction chemistry for electrochemical glycerol oxidation by atomic-layer-deposited Pt-nanoparticle catalysts, *Appl. Catal. B: Environ.* 273 (2020), 119037, <https://doi.org/10.1016/j.apcatb.2020.119037>.
- [30] Y. Zhao, L. Zhang, J. Liu, K. Adair, F. Zhao, Y. Sun, T. Wu, X. Bi, K. Amine, J. Lu, X. Sun, Atomic/molecular layer deposition for energy storage and conversion, *Chem. Soc. Rev.* 50 (2021) 3889–3956, <https://doi.org/10.1039/D0CS00156B>.
- [31] M. Jia, N. Zhao, H. Huo, X. Guo, Comprehensive investigation into garnet electrolytes toward application-oriented solid lithium batteries, *Electrochem. Energy Rev.* 3 (34) (2020) 656–689, <https://doi.org/10.1007/S41918-020-00076-1>.
- [32] W.W. McNear, S.F. Zaccarine, A. Lai, A.E. Linico, S. Pylypenko, A.W. Weimer, Improved durability and activity of Pt/C catalysts through atomic layer deposition of tungsten nitride and subsequent thermal treatment, *Appl. Catal. B: Environ.* 254 (2019) 587–593, <https://doi.org/10.1016/j.apcatb.2019.05.036>.
- [33] H.-B.-R. Lee, S.F. Bent, Microstructure-dependent nucleation in atomic layer deposition of Pt on TiO<sub>2</sub>, *Chem. Mater.* 24 (2012) 279–286, <https://doi.org/10.1021/cm202764b>.
- [34] B.C. Beard, P.N. Ross, Platinum-titanium alloy formation from high-temperature reduction of a titania-impregnated platinum catalyst: implications for strong metal-

- support interaction, *J. Phys. Chem.* 90 (1986) 6811–6817, <https://doi.org/10.1021/j100284a020>.
- [35] K. Shinozaki, J.W. Zack, R.M. Richards, B.S. Pivovar, S.S. Kocha, Oxygen reduction reaction measurements on platinum electrocatalysts utilizing rotating disk electrode technique, *J. Electrochem. Soc.* 162 (2015) F1144–F1158, <https://doi.org/10.1149/2.1071509jes>.
- [36] Y. Garsany, O.A. Baturina, K.E. Swider-Lyons, S.S. Kocha, Experimental methods for quantifying the activity of platinum electrocatalysts for the oxygen reduction reaction, *Anal. Chem.* 82 (2010) 6321–6328, <https://doi.org/10.1021/ac100306c>.
- [37] B. Ravel, M. Newville, IUCr, ATHENA, ARTEMIS, HEPHAESTUS: data analysis for X-ray absorption spectroscopy using IFEFFIT, *J. Synchrotron Radiat.* 12 (2005) 537–541, <https://doi.org/10.1107/S0909049505012719>.
- [38] P.E. Blöchl, Projector augmented-wave method, *Phys. Rev. B. Condens. Matter* 50 (1994) 17953–17979.
- [39] J.J. Mortensen, L.B. Hansen, K.W. Jacobsen, Real-space grid implementation of the projector augmented wave method, *Phys. Rev. B* 71 (2005), 035109, <https://doi.org/10.1103/PhysRevB.71.035109>.
- [40] J. Wellendorff, K.T. Lundgaard, A. Møgelhøj, V. Petzold, D.D. Landis, J.K. Nørskov, T. Bligaard, K.W. Jacobsen, Density functionals for surface science: exchange-correlation model development with Bayesian error estimation, *Phys. Rev. B* 85 (2012), 235149, <https://doi.org/10.1103/PhysRevB.85.235149>.
- [41] G. Houchins, V. Viswanathan, Quantifying confidence in density functional theory predictions of magnetic ground states, *Phys. Rev. B* 96 (2017), 134426, <https://doi.org/10.1103/PhysRevB.96.134426>.
- [42] V. Sumaria, D. Krishnamurthy, V. Viswanathan, Quantifying confidence in DFT predicted surface pourbaix diagrams and associated reaction pathways for chlorine evolution, *ACS Catal.* 8 (2018) 9034–9042, <https://doi.org/10.1021/acscatal.8b01432>.
- [43] A.J. Medford, J. Wellendorff, A. Vojvodic, F. Studt, F. Abild-Pedersen, K. W. Jacobsen, T. Bligaard, J.K. Nørskov, Catalysis. Assessing the reliability of calculated catalytic ammonia synthesis rates, *Science* 345 (2014) 197–200, <https://doi.org/10.1126/science.1253486>.
- [44] Z. Ahmad, V. Viswanathan, Quantification of uncertainty in first-principles predicted mechanical properties of solids: application to solid ion conductors, *Phys. Rev. B* 94 (2016), 064105, <https://doi.org/10.1103/PhysRevB.94.064105>.
- [45] D. Krishnamurthy, V. Sumaria, V. Viswanathan, Maximal predictability approach for identifying the right descriptors for electrocatalytic reactions, *J. Phys. Chem. Lett.* 9 (2018) 588–595, <https://doi.org/10.1021/acs.jpclett.7b02895>.
- [46] K. Shinozaki, J.W. Zack, S. Pylypenko, B.S. Pivovar, S.S. Kocha, Oxygen reduction reaction measurements on platinum electrocatalysts utilizing rotating disk electrode technique: II. Influence of ink formulation, catalyst layer uniformity and thickness, *J. Electrochem. Soc.* 162 (2015) 1384–1396, <https://doi.org/10.1149/2.0551512jes>.
- [47] L.K. Ono, B. Yuan, H. Heinrich, B. Roldan Cuenya, Formation and thermal stability of platinum oxides on size-selected platinum nanoparticles: support effects, *J. Phys. Chem. C* 114 (2010) 22119–22133, <https://doi.org/10.1021/jp1086703>.
- [48] Y. Lei, H. Zhao, R.D. Rivas, S. Lee, B. Liu, J. Lu, E. Stach, R.E. Winans, K. W. Chapman, J.P. Greeley, J.T. Miller, P.J. Chupas, J.W. Elam, Adsorbate-induced structural changes in 1–3 nm platinum nanoparticles, *J. Am. Chem. Soc.* 136 (2014) 9320–9326, <https://doi.org/10.1021/ja4126998>.
- [49] R. Christensen, H.A. Hansen, C.F. Dickens, J.K. Nørskov, T. Vegge, Functional independent scaling relation for ORR/OER catalysts, *J. Phys. Chem. C* 120 (2016) 24910–24916, <https://doi.org/10.1021/acs.jpcc.6b09141>.
- [50] S. Kattel, Z. Duan, G. Wang, Density functional theory study of an oxygen reduction reaction on a Pt<sub>3</sub>Ti alloy electrocatalyst, *J. Phys. Chem. C* 117 (2013) 7107–7113, <https://doi.org/10.1021/jp400158r>.